Vibronic Analysis of the S-1-S-0 Transition of Phenylacetylene Using Photoelectron Imaging and Spectral Intensities Derived from Electronic Structure Calculations

ARTICLE *in* THE JOURNAL OF PHYSICAL CHEMISTRY A · AUGUST 2010

Impact Factor: 2.69 · DOI: 10.1021/jp103449r · Source: PubMed

4 AUTHORS, INCLUDING:

Chih-Hsuan Chang
CiS Forschungsinstitut für Mikrosensorik u…
16 PUBLICATIONS **45** CITATIONS
SEE PROFILE

Gary V. Lopez
Brown University
24 PUBLICATIONS **107** CITATIONS
SEE PROFILE

Trevor Sears
Brookhaven National Laboratory
180 PUBLICATIONS **3,538** CITATIONS
SEE PROFILE

Vibronic Analysis of the S_1-S_0 Transition of Phenylacetylene Using Photoelectron Imaging and Spectral Intensities Derived from Electronic Structure Calculations

Chih-Hsuan Chang,[†,‡] Gary Lopez,[†] Trevor J. Sears,[†,‡] and Philip M. Johnson*[,†]

Departments of Chemistry, Stony Brook University, Stony Brook, New York 11794-3400, and Brookhaven National Laboratory, Upton, New York 11973-5000

Received: April 16, 2010; Revised Manuscript Received: June 21, 2010

The vibrational structure of the S_1-S_0 electronic band of phenylacetylene has been recorded by 1 + 1 resonance-enhanced multiphoton ionization, accompanied by slow electron velocity map imaging photoelectron spectroscopy at each resonant vibrational band. Assignments of the S_1 vibrations (up to 2000 cm^{-1} above the band origin) are based upon the relative intensities of the vibronic bands calculated by complete second-order vibronic coupling, vibration−rotation (Coriolis and Birss) coupling calculations, and the vibrational structure of the S_1 resonant photoelectron spectra. Although this is an allowed electronic transition, the relative intensities of the a_1 bands are often largely determined by vibronic coupling rather than simple Franck−Condon factors, and second-order coupling is substantial. Nonsymmetric vibrations have intensities obtained through either vibronic or Coriolis coupling, and the calculations have been instrumental in discriminating between alternate possibilities in the assignments. Strong vibronic effects are expected to be present in the spectra of most monosubstituted benzenes, and the calculations presented here show that theoretical treatments based upon electronic structure calculations will generally be useful in the analysis of their spectra.

Introduction

Vibronic character in a molecular optical transition is commonly associated with those that are forbidden by symmetry. However, it has long been known[1−3] that vibronic activity can also occur in an allowed transition and indeed can occur in *any* molecular spectrum. While in forbidden transitions intensity can only be induced by nonsymmetric vibrations, in formally allowed transitions one has the additional feature that symmetric vibrations are fully capable of providing additional oscillator strength.

In strongly allowed electronic bands, vibronic effects are weak in comparison to the strength of the direct excitation, but there are certain classes of molecular transitions that have minimal direct oscillator strength and where vibronic effects may dominate. Electronic bands can be weak because of too much change in the nodal structure between the upper and lower states, because of minimal spatial overlap between the upper and lower molecular orbitals, or because of interference effects resulting from configuration interaction. Aromatic molecules provide many examples of the latter situation.

Because of the near symmetry of π molecular orbital energies above and below the midpoint between the HOMO and LUMO in aromatics, there are many cases of near-degenerate orbital excitation. Configuration interaction is especially strong for those degenerate excitations, and one can think of taking plus and minus combinations of the resulting configurations. Calculating the transition moments from the minus combination results in a cancellation of the moments of the individual transitions, giving a weak electronic band, while the plus combination gives a strong band of the same symmetry. In many aromatics such as substituted benzenes and naphthalene, the minus combination results in S_1 and the plus combination is the upper state S_3. The weak S_1 transitions in these molecules provide fertile ground for the study of vibronic effects in formally allowed transitions.

In a previous paper,[4] we discussed the use of modern quantum mechanical programs for calculating vibronic coupling without the use of perturbation theory. Using the derivatives of the transition moments in Taylor's expansion of the transition moments and Franck−Condon factors allowed vibronic oscillator strengths to be obtained directly. As applied to a forbidden transition of benzonitrile cation, it was shown that including the second order in the expansion was important for including combination bands in the spectrum and that spectra could be simulated with enough fidelity to be of great assistance in analyzing the vibrational structure of the transition.

Because of much greater configuration interaction in the S_1 state of a substituted benzene than in a cation state, and because of the allowed character of a transition from the neutral ground state, a vibronic analysis of the $S_1(\tilde{A}^1B_2) \leftarrow S_0(\tilde{X}^1A_1)$ transition of a substituted benzene provides a greater challenge than one for the benzonitrile cation transition. Here we treat the phenylacetylene molecule, comparing a more thorough vibronic calculation to the jet-cooled resonance-enhanced multiphoton ionization (REMPI) $S_1 \leftarrow S_0$ spectrum. To provide more information for vibrational assignments, velocity map imaging photoelectron spectra were also recorded for the resonant ionization process through the vibrational features of the spectrum.

In addition to being a good candidate for a test of calculational methods, phenylacetylene was chosen to gather more information about the character of its S_1 state. It has recently been discovered that there is an anomalous photochemical transformation that occurs in this molecule when excited to S_1.[5] Although there is strong fluorescence, about 20% of the excitations immediately result in the formation of a species with a low ionization potential and a lifetime exceeding 100 μs. The identity of this photoproduct has not yet been determined, and if the vibrational structure of S_1 were accurately known, a study

* To whom correspondence should be addressed.
† Stony Brook University.
‡ Brookhaven National Laboratory.

10.1021/jp103449r
Published on Web 07/22/2010

of the photoproduct formation as a function of the vibrational level might provide some clues to this identity.

Vibronic and Vibration−Rotation Calculations

The method used to calculate vibrational intensities has been described previously,[4] and the basics are reproduced here for clarity.

In the Born−Oppenheimer approximation, the wave function of a particular electronic-vibrational state can be written as a product of the electronic function ψ with a vibrational function χ, which are dependent upon the electronic coordinates q and the nuclear coordinates Q:

$$\Psi(q, Q) = \psi(q, Q)\,\chi(Q) \tag{1}$$

The intensity of any particular vibronic transition is proportional to the square of the transition moment M between the upper and lower states:

$$M_{\mathrm{ul}} = \langle \psi_{\mathrm{u}}\chi_{\mathrm{u}}|\boldsymbol{\mu}|\psi_{\mathrm{l}}\chi_{\mathrm{l}}\rangle \tag{2}$$

where $\boldsymbol{\mu}$ is the dipole moment operator and the integration is over all electronic and nuclear coordinates.

To describe the vibrations, the nuclear coordinates can be expressed in terms of vectors in the displacements of each atom from its equilibrium nuclear position, giving rise to a set of normal coordinates $\{\mathbf{Q}_i\}$ appropriate to the nuclear force field. The vibrational wave functions are then simply the products of harmonic oscillator functions along each normal coordinate. Since the force fields and the equilibrium positions of two electronic states can be different, one must distinguish two different coordinate sets, $\{\mathbf{Q}_i'\}$ and $\{\mathbf{Q}_i''\}$, for the two states. These sets are related by the Duschinsky transformation $\mathbf{Q}' = \mathbf{J}\mathbf{Q}'' + \mathbf{K}$, where $\mathbf{J}$ is a rotation matrix and $\mathbf{K}$ is a geometry displacement vector.[6]

Integrating over the electronic coordinates provides a geometry-dependent transition moment $M(Q)$, and integration of this over the vibrational wave functions gives the transition moment for an individual vibronic band, M_{ul}:

$$M_{\mathrm{ul}} = \langle \chi_{\mathrm{u}}(Q')|M(Q)|\chi_{\mathrm{l}}(Q'')\rangle \tag{3}$$

The transition moment could be obtained by calculating $M(Q)$ with an electronic structure program at various geometries on the normal coordinate hypersurface and numerically integrating over the vibrational wave functions. Since the normal coordinate space has $3N - 6$ dimensions, it is more practical to express $M(Q)$ as a Taylor expansion in the normal coordinates for each polarization direction:

$$M(Q) = M(0) + \sum_i \left(\frac{\partial M}{\partial Q_i}\right)_0 Q_i + {}^1/_2 \sum_{i,j} \left(\frac{\partial^2 M}{\partial Q_i\,\partial Q_j}\right)_0 Q_i Q_j + {}^1/_6 \sum_{i,j,k} \left(\frac{\partial^3 M}{\partial Q_i\,\partial Q_j\,\partial Q_k}\right)_0 Q_i Q_j Q_k + \ldots \tag{4}$$

As shown previously,[4] the terms of the moment expansion may be reduced to sums of vibrational overlap integrals times the derivatives of the transition moments by use of the recursion relation for Hermite polynomials.

In our previous work, only the vibrations expected to appear in the spectrum were considered. Here a more general approach was taken and moment derivatives were calculated to second order (all that is needed in C_{2v} symmetry[4]) for all of the non-CH stretch vibrations. For phenylacetylene (PA), that means 30 vibrations, 22 of which are inducing modes for $S_1 \leftarrow S_0$. The derivatives were determined from finite differences between the electronic transition moments calculated at various points along each of the normal modes for the first derivatives and also at simultaneous excursions along each pair of normal modes for the second derivatives. A matrix of second derivatives is called a Hessian, and the moment Hessians were determined for each vibrational level.

The vibrational frequencies and vectors were calculated using MCSCF (eight electrons in an eight-orbital active space) with the Dunning aug-cc-pVDZ basis set in the GAMESS electronic structure package. The $S_1 \leftarrow S_0$ transition energy for this method was 35 812 cm^{-1} when corrected for the zero-point energies, only 63 cm^{-1} higher than the experimental value. The electronic transition moments were calculated using time-dependent density functional theory (TDDFT) also in GAMESS with the same basis set. Around 1500 points in the vibrational hyperspace were sampled. A serious issue in the use of TDDFT for transition moment derivatives is that the signs of the transition moments are not defined and are random from run to run. The proper relative signs of the derivatives are very important in eq 4, however. A consistent set of signs were developed by arbitrarily setting the sign for the first derivative for one vibration in the calculation for each polarization direction. Then the signs for all the other moment values were fixed by requiring continuity of moments and their derivatives as a function of nuclear geometry. This required somewhat more points to be considered than otherwise would have been necessary for the determination of derivatives when the signs are known.

Input files for each calculation were generated from the vibrational vectors by a computer program, and these were submitted automatically to a 16-processor computer by a Linux shell script, which also extracted the desired moments from the output files.

Intensities were calculated for every symmetry-viable vibrational level up to about 2000 cm^{-1} ($\sim$10 000 states). This required $\sim 10^7$ Franck−Condon factors that were provided by the MolFC program, developed and distributed by R. Borrelli and A. Poluso.[7]

Figure 1 displays the variations of the *y*-polarized (in-plane, perpendicular to the acetylene axis) transition moments along some of the normal coordinates. This is the polarization that is active for the allowed component of the electronic transition. It is seen, therefore, that the curves all cross the equilibrium geometry at an offset that is the purely allowed value. The curves are found to be purely linear for the a_1 vibrations and purely parabolic for all other symmetries, stemming from the fact that a_1 is the inducing symmetry for this polarization. Vibronic mode moments have to be odd functions with respect to Q, while nonvibronic modes must be even. The appearance of these curves makes apparent why there is considerable vibronic character, even in the a_1 modes. For many of the vibrations, the transition moments away from equilibrium are much larger than the value at equilibrium. Overlapping these curves with harmonic oscillator wave functions and integrating (as in eq 3) will include these areas of greater transition probability and potentially increase the oscillator strength.

Figure 2 shows a simulation of only the *y*-polarized spectrum showing the effects of including various terms in Taylor's

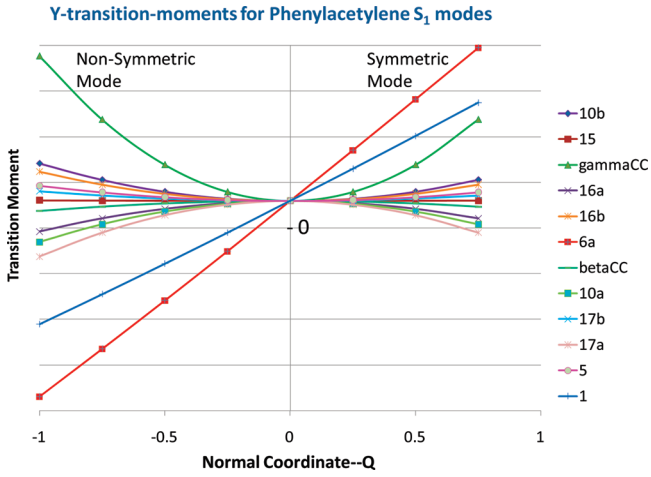

Figure 1. *y* transition moments for various vibrational modes as a function of the normal coordinate position. a_1 symmetry modes are linear, while all others have a quadratic dependence on *Q*.

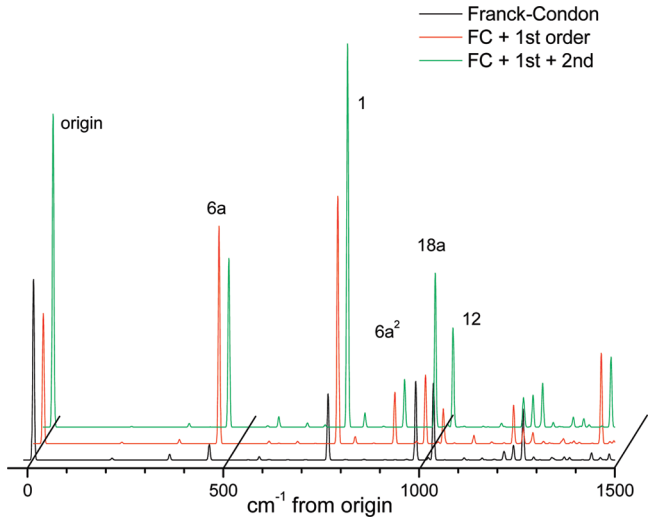

Figure 2. Simulation of the a_1 bands of the S_1 spectrum as a function of the order of vibronic coupling included. The left peaks are with only Franck−Condon factors considered, while the center peaks (red) also include first-order vibronic coupling, and the right peaks (green) include vibronic coupling to second order.

expansion. As shown in the left spectrum, the pure electronic transition moment at the equilibrium geometry is split up into the various a_1 modes by the Franck−Condon factors. Adding a first-order vibronic correction actually decreases the origin band because of interference,[8] but greatly enhances most of the other modes. The second-order contribution provides a big boost to the origin because the nonsymmetric zero-point vibrations explore regions of larger transition moment and enhance some modes while having little effect on others. Table 1 shows the effects of the different orders on the overall spectra. For the *y* polarization, the first-order contribution is about 1.4 times the allowed part, and the second-order contribution is about equal to it. There is of course no allowed character in the *x* and *z* polarizations, and the *x* intensity (out-of-plane) is negligible.

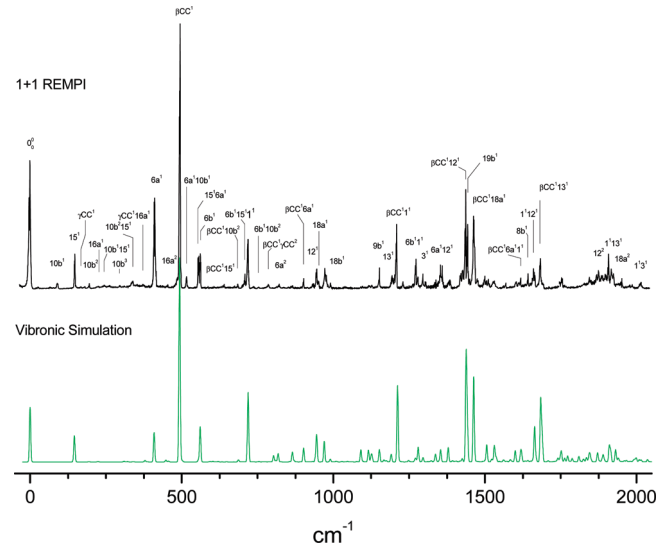

Figure 3. (Top) 1 + 1 REMPI spectrum of phenylacetylene resonant with the S_1 state. (Bottom) Simulation of the S_1-S_0 transition with the assignment of some vibrational levels, using experimental vibrational frequencies.

However, the first-order *z*-polarized vibronic effects mixing in the nearby $^1A_1$ S_2 state are very strong, providing 88% of the total calculated intensity for the entire transition. The second-order contribution to the *z*-polarized spectrum is relatively small, but it cancels rather than adds to the overall sum. As such it overwhelms the positive second-order contributions to the other polarizations, and there is accidentally almost no second-order effect on the overall transition intensity although some individual bands exhibit large second-order intensity changes.

Figure 3 presents a comparison of a combination of all the simulated spectra to the experimental REMPI spectrum of S_1. For the most part the comparison is satisfying. However, to get this agreement, the *y*-polarized intensities (a_1 modes) were scaled up by a factor of 3.55. It is not clear whether this variance is due to theoretical or experimental artifacts. When peak heights are measured, as is done here, a difference in rotational band contours between symmetries can cause a consistent bias toward one polarization or another. As shown by King and So,[15] there is a large difference between the band contours for the a_1 vibrations and the b_2 vibrations, with the former having two substantially separated band heads while the latter only has one. The a_1 contours are thus broader, and a substantial portion of the scaling factor is probably due to this bias. Also, since this is a resonance ionization spectrum, the experimental intensities depend upon both $S_1 \leftarrow S_0$ and the ionization transition. It is entirely possible that the ionization cross-section for *z* polarization is stronger than that of the *y* polarization, resulting in an enhancement of the experimental b_2 vibrations. However, the relative intensities in the REMPI spectrum do not differ much from those of the fluorescence excitation spectrum of Powers, Hopkins, and Smalley,[9] so while they may contribute, the ionization cross sections are probably not the major cause of this factor. On the theoretical side, unless there is some universal bias in the TDDFT calculations for the *z* moments, it is difficult

TABLE 1: Effects of Different Vibronic Orders on the Overall Intensity of the Phenylacetylene $S_1 \leftarrow S_0$ Transition

	y polarization	*z* polarization	*x* polarization	all
zeroth order only	8.9×10^{-5}	0	0	8.9×10^{-5}
zeroth + first order	2.15×10^{-4}	2.38×10^{-3}	2.56×10^{-6}	2.60×10^{-3}
zeroth + first + second order	3.00×10^{-4}	2.29×10^{-3}	3.76×10^{-6}	2.60×10^{-3}

to see how errors in the vibronic calculation could affect a whole polarization fairly uniformly.

While the vibronic intensities reported here include all of the effects of electronic-vibrational coupling within the Born−Oppenheimer approximation, they do not include the effects of coupling between adiabatic Born−Oppenheimer states induced by nuclear momenta. As pointed out by Orlandi and Siebrand,[10] and seen in the naphthalene spectrum,[11] this coupling can be of substantial magnitude and produce similar vibrational structure, but with altered intensities. It will have to be investigated further whether Born−Oppenheimer coupling could explain the increased experimental intensities of the a_1 vibrations as compared to the vibronic calculations.

It is apparent in the comparison between the experimental and the simulated spectra that there are several weak experimental bands missing in the simulation because of symmetry (transitions to S_1 vibrations of b_1 symmetry are forbidden from the vibrationless ground state). The major cause of symmetry breakdown in gas-phase electronic spectra is vibration−rotation coupling, arising from the changes in inertial moments during a vibration (Coriolis coupling) and changes in the vibrational potential caused by centrifugal distortions from the rotations (Birss coupling).

Perturbation operators for the lowest orders of these two effects are[12]

$$T_{\text{Coriolis}} = -\sum_{\alpha,r,s} \mu^{\text{e}}_{\alpha\alpha}\zeta^{\alpha}_{rs}Q_r\hat{P}_s\hat{J}_\alpha \tag{5}$$

and

$$T_{\text{Birss}} = {}^3/_8 \sum_{\alpha,\beta,\gamma,r,s} \mu^{\text{e}}_{\alpha\alpha}\alpha^{\alpha\gamma}_r\mu^{\text{e}}_{\gamma\gamma}\alpha^{\gamma\beta}_s\mu^{\text{e}}_{\beta\beta}Q_rQ_s\hat{J}_\alpha\hat{J}_\beta \tag{6}$$

where $\mu_{\alpha\alpha} = 1/I_{\alpha\alpha}$ is a diagonal element of the inverse inertial tensor, ζ^{α}_{rs} is a Coriolis coefficient, $\alpha^{\alpha\beta}_r = (\partial I_{\alpha\beta}/\partial Q_r)_{\text{e}}$ is the change in an inertial element due to a vibration, Q_r is the rth mass-weighted normal coordinate, and $\hat{J}_\alpha$ is the rotational operator for the α inertial axis.

For coupling between a vibration with $v = 1$ and other pure $v = 0$ fundamentals, the matrix elements for these operators are

$$\langle T_{\text{Coriolis}}\rangle_{r,s} = \frac{i\hbar}{2}\sum_{\alpha}\mu^{\text{e}}_{\alpha\alpha}\zeta^{\alpha}_{rs}\left[\left(\frac{\tilde{\omega}_s}{\tilde{\omega}_r}\right)^{1/2} + \left(\frac{\tilde{\omega}_r}{\tilde{\omega}_s}\right)^{1/2}\right]\langle\hat{J}_\alpha\rangle \tag{7}$$

and

$$\langle T_{\text{Birss}}\rangle_{r,s} = \frac{3}{64\pi^2c^2}\sum_{\alpha,\beta,\gamma}(\mu^{\text{e}}_{\alpha\alpha}\alpha^{\alpha\gamma}_r\mu^{\text{e}}_{\gamma\gamma}\alpha^{\gamma\beta}_s\mu^{\text{e}}_{\beta\beta} + \mu^{\text{e}}_{\alpha\alpha}\alpha^{\alpha\gamma}_s\mu^{\text{e}}_{\gamma\gamma}\alpha^{\gamma\beta}_r\mu^{\text{e}}_{\beta\beta})\left(\frac{1}{\tilde{\omega}_r\tilde{\omega}_s}\right)^{1/2}\langle\hat{J}_\alpha\hat{J}_\beta\rangle \tag{8}$$

where $\tilde{\omega}$ is a vibrational frequency (cm^{-1}), while $\langle\hat{J}_\alpha\rangle$ and $\langle\hat{J}_\alpha\hat{J}_\beta\rangle$ are the matrix elements of the angular momentum operators. In these equations, the output and the input vibrational energies are in wavenumbers, and in eq 8 all of the quantities must be calculated in cgs units to maintain consistency with cm^{-1}.

The individual contributions to the above equations can all be extracted from the results of electronic structure calculations, and the resulting matrices can be manipulated to give energy shifts and the coefficients for the expansion of state vibrational functions in terms of a harmonic oscillator basis. The resulting coefficients determine the state mixing and therefore provide a means to estimate the intensities of bands that are made allowed by vibration−rotation interaction. As an example, the wave function vectors are listed in Table 2 for both Coriolis and Birss coupling between the 10b and 15 modes in S_1 phenylacetylene.

Since the Birss coupling results from a higher order term in the expansion of the inertial moments in terms of the normal coordinates, it is expected to yield smaller coupling coefficients than the Coriolis effect. Table 2 shows that is indeed the case and that the Birss term usually couples different vibrations compared to the Coriolis term. Since the intensities are proportional to the square of these coefficients, Birss coupling in phenylacetylene can be taken to be negligible.

In Coriolis coupling for a symmetric rotor, the z axis coupling is proportional to K, and for the other axes T_{Coriolis} is about proportional to $(J^2 - K^2)^{1/2}$. Therefore, the coupling varies greatly over a Boltmann distribution of rotational states, and the effect of the coupling is temperature dependent. The couplings in Table 2 are averaged over the distribution at a temperature of 30 K. Band contours are also affected by the Coriolis coupling, and a vibrational band made allowed by it has enhanced intensities at higher J and K values. Likewise, bands that lose intensity by this mechanism will lose it mostly at higher J and K values.

Experiment

The experimental apparatus used for this study has been previously described[5] except for recent modifications of the ion optics for velocity mapping imaging. The PA (98%) purchased from Aldrich was used without any purification. The sample, with He as the carrier gas, was supersonically expanded through a general pulsed valve (300 μm orifice diameter) running at 10 Hz. The helium backing pressure was optimized at roughly 200 Torr by optimizing the quality of the electron imaging and ensuring the absence of dimers in the TOF mass spectrum. After collimation by the skimmer with a 3 mm diameter, the PA beam enters the interaction region midway between the repeller and extractor plates.

The ion optics setup is derived from that of Townsend et al.[13] and only mentioned briefly here. It consists of four electrode plates with inner diameters of 3, 5, 10, and 15 mm. The outer diameters of these plates are 45 mm, and they have a 1 mm thickness. Before the experiment, the electric field's flatness and focusing condition were simulated by Simion software and the resolution was limited by the pixel number. The voltages for these plates were provided by a high-voltage power supply, divided by a series of resistors to power the various electrodes. The whole ion optics and field-free time-of-flight (TOF) region was shielded by a μ-metal tube to avoid any distortion from background residual magnetic fields. The detector includes 75 mm chevron-type microchannel plates (MCPs; Photonis USA, Inc.), a phosphor, and a video camera (XC-ST50, Sony).

A pulsed Nd:YAG laser (YG580, Quantel) was used to pump the dye laser. The output of the dye laser was doubled in a BBO crystal housed in an Inrad autotracker and directed into the detection chamber in the direction opposite that of the molecular beam. The resulting ions were projected onto the MCP detector, and the fluorescence from the phosphor was captured by the camera and then transferred to a PC for storage and further analysis. Calibration of the fundamental wavelength was done with a wavemeter (WaveMaster, Coherent). The time

TABLE 2: Coefficients of the Harmonic Normal Mode Basis Functions for Modes 10b and 15 after Mixing by Rotation−Vibration Coupling[a]

	mode			wave function coefficient			
				z axis Coriolis		Birss	
	frequency (cm^{-1})	symmetry	label	10b	15	10b	15
1	97	b_1	10b	0.99948		1	
2	146	b_2	15	0.03198	0.99939	0	1
3	168	b_1	γCC	0.00032	0.01353	0	1.2×10^{-6}
4	224	a_2	16a	0	0	4.26×10^{-5}	9×10^{-7}
5	277	b_1	16b	0.00005	0.00385	0	3×10^{-7}
6	388	b_1	γCH	0.00003	0.0008	0	3×10^{-7}
7	409	a_1	6a	0	0	5.4×10^{-6}	2×10^{-7}
8	464	b_1	4	0.00001	0.00027	0	1×10^{-7}
9	493	b_2	βCC	0.00141	0	0	1×10^{-7}
10	527	b_1	11	0.00001	0.00004	1.62×10^{-5}	0
11	554	a_2	10a	0	0	0	3×10^{-7}
12	561	b_2	6b	0.00192	0.00001	0	1×10^{-7}
13	588	b_1	17b	0.00002	0.00003	9.7×10^{-6}	0
14	624	a_2	17a	0	0	0	0
15	666	b_1	5	0	0.00002	0	1×10^{-7}
16	719	a_1	1	0	0	1.54×10^{-5}	0
17	708	b_2	βCH	0.00153	0	0	1×10^{-7}
18	945	a_1	12	0	0	0	1×10^{-7}
19	990	b_2	18b	0	0	0	0
20	970	a_1	18a	0.00062	0	0	0
21	1126	a_1	9a	0	0	0	1×10^{-7}
22	1152	b_2	9b	0.00064	0	0	1×10^{-7}
23	1191	a_1	13	0	0	0	0
24	1296	b_2	3	0.00027	0	0	1×10^{-7}
25	1366	b_2	14	0.00004	0	1.6×10^{-6}	0
26	1419	a_1	19a	0	0	0	0
27	1442	b_2	19b	0.00008	0	0	0
28	1539	a_1	8a	0	0	1.4×10^{-6}	0
29	1642	b_2	8b	0.00022	0	0	0
30	2023	a_1	νCC	0	0	0	0

[a] Experimental frequencies were used when available; otherwise those from the current calculations were adopted. The Coriolis and Birss couplings were considered independently.

sequence of the pulsed valve, laser system, and camera was controlled by delay generators (DG535, Stanford Research System) and PC-mounted timer cards. The data collection was programmed by LabVIEW software, using a National Instruments frame grabber.

The REMPI photoelectron images were recorded while scanning a dye laser over the S_1 transition. The sensitivity of the method makes it possible to record PE spectra continuously while scanning the laser over the transition, providing a 2D spectrum. The REMPI spectrum is then obtained by integrating the electron imaging data set collected for each wavelength. However, for more detailed analyses of the electron images, the laser was reduced in power and tuned to the center of a vibrational line, collecting roughly 5000 shots per image. Space charge effects were thereby minimized. A representative sample of photoelectron spectra from S_1 REMPI is shown in Figure 4.

The analysis of electron imaging was performed with the qBASEX program developed by Dribinski et al.[14] To display the photoelectron spectra, the radial coordinates of the images were converted to kinetic energy, integrated over the angular coordinate, and corrected with a Jacobian factor.

The angular distribution of electrons from a 1 + 1 REMPI scheme is described by the equation

$$I(\theta) = 1 + \beta_2 P_2(\cos\theta) + \beta_4 P_4(\cos\theta) \qquad (9)$$

In this case, the β_4 parameter, as compared to the variance in the fitting process, had a minor or insignificant effect on the angular distribution and was constrained to zero in the final fitting process. On the basis of the assumption of a one-photon process, the limiting values of the β_2 anisotropic parameters are $-1 \leq \beta_2 \leq +2$, indicating the angular distributions of the fragments in the laboratory space are perpendicular and parallel to the polarization of the excitation laser field. If the fitting parameter is close to zero, the distribution tends to be isotropic. Most of the values of the anisotropic parameter (β_2) range from 0.2 to 0.7 in this study, indicating weak anisotropy. The more anisotropic patterns in general occurred for higher energy electrons and for those resulting from excitation of a 6a-containing mode in S_1, but the results were not consistent enough for anisotropy to be used as a tool for state assignments.

While it was attempted to make the relative experimental intensities in the REMPI spectrum as meaningful as possible, the fact that the study was done with a dye laser using several dyes makes complete accuracy impossible. The presented spectrum is a composite of overlapping spectra from several dyes, and for each the dye laser changes in intensity and mode structure as it is scanned, having effects on the intensities. The spectra from adjacent individual dyes were scaled by making a band appearing in both spectra have the same intensity before the spectra were spliced. However, the intensities also vary across a dye range, and the splicing is therefore not necessarily a uniquely defined process.

Results and Discussion

All vibrational analysis of the S_1 spectrum of phenylacetylene is built upon the fundamental work of King and So,[15] who

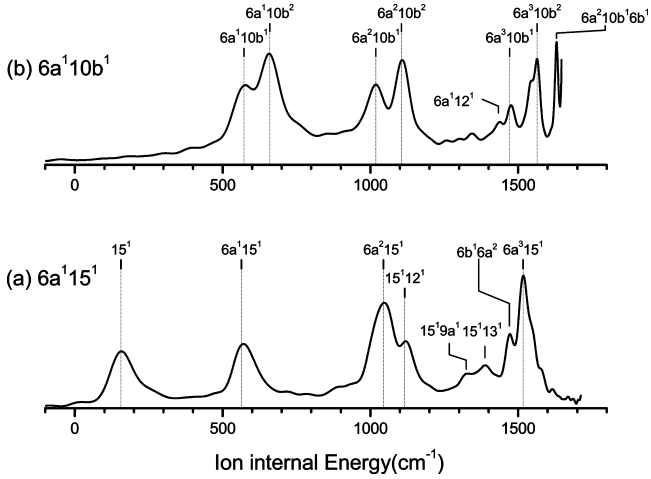

Figure 4. Selection of photoelectron spectra from two-photon transition resonance with various vibrational states of S_1 phenylacetylene. The S_1 vibrational labels are at the left of each trace, and suggested ionic vibrational assignments are at the top.

analyzed the room temperature absorption spectrum using isotopic substitution and band contour analysis. Subsequently, Powers, Hopkins, and Smalley recorded the fluorescence excitation spectrum of the jet-cooled molecule,[9] Chia and Goodman measured the room temperature two-photon spectrum,[16] and both Narayanan et al.[17] and Philis, Drougas, and Kosmas[18] analyzed the 1 + 1 REMPI jet-cooled spectrum. Theoretical calculations through the years have culminated in a thorough treatment by Serrano-Andres, Merchan, and Jablonski using CASSCF and CASPT2 methods,[19] providing good estimates for the vibrational frequencies. In the present study a requirement of consistency with both the vibrational structure in the photoelectron spectra and the intensities in the vibronic calculations enables a more extensive and reliable assignment of the vibrational transitions in the S_1 spectrum.

Figure 3 shows a 1 + 1 REMPI spectrum of PA in the range of 0−2000 cm^{-1}, with some assignments of vibrational levels in the S_1 state. Also displayed is a simulation of the spectrum using intensities from the vibronic calculation. The simulated spectrum agrees well with the experimental spectrum, indicating the validity of the assignments.

Due to the low density of states, most assignments of the vibrational levels at low excitation energy are clear. As the excitation energy increases, more congestion appears, and in many cases it is impossible to clearly assign the features without ambiguity using only theoretical frequencies. The vibrations below 2000 cm^{-1} are all various types of CC stretching, CC bending, and ring deformation modes. The point group of PA is C_{2v}, and there are totally 36 nondegenerate normal modes, 13 of which belong to a_1 symmetry, 3 to a_2, 8 to b_1, and 12 to b_2. The S_1 state has an electronic symmetry of B_2, resulting in $S_1 \leftarrow S_0$ having allowed transitions from the S_0 origin to a_1, a_2, and b_2 vibrations of S_1. S_1 is allowed but weak because it derives from the forbidden $^1B_{2u}$ state of benzene, but it can gain intensity by coupling to nearby strongly allowed A_1 and B_2 states through b_2 and a_1 vibrations.

There are two conventional labeling schemes for the vibrations in aromatic compounds. We have adopted Wilson's notation,[20] rather than Herzberg's, to designate the vibrations in the text because it is more consistent between states of the molecule and between the various substituted benzenes. Conversion can be made by referring to Table 3. The vibrational modes and symmetries for S_1 are summarized in Table 3, many of which were used as the resonance intermediate levels in the photoelectron imaging experiment.

The electronic origin of the S_1 state in this work is determined to be 35 875 cm^{-1}, close to the 35 877.18 cm^{-1} measured by Ribblett et al., from the high-resolution, rotationally resolved spectrum.[21] This difference is reasonable because here the rotational structure is not resolved and the position of the peak intensity is reported, corresponding to a band head, not the band origin.

The vibrational modes involved in the transitions below 800 cm^{-1} are dominated by the modes 15, 6a, βCC, 6b, and 1, with vibrational energies 147, 409, 494, 561, and 719 cm^{-1}, respectively. Most strong transitions involving these modes have been assigned in previous studies, and they need not be discussed further. The symbol β indicates in-plane oscillation of the atoms in the acetylene group, and βCC primarily involves motion of the carbon nearest the ring. This vibration has the most vibronic strength and thus shows most strongly in the spectrum.

The lower intensity bands are much more of a challenge to our understanding, and Figure 5 shows an expanded version of the experimental spectrum so the weak bands can be seen. For the upper, lower energy trace the vertical axis is expanded by a factor of 10, and for the higher energy portion of the spectrum the scale is expanded 3-fold.

One of the more interesting weak bands in the lower part of the spectrum is the first one seen with significant intensity at 97 cm^{-1}. This fundamental frequency was ascribed to the 10b vibration by Narayanan et al.[17] by virtue of their vibrational calculations and the appearance of the $10b^2$ band in the spectrum. The problem with its appearance as $10b^1$ in the REMPI spectrum is that its symmetry is b_1, so it should be forbidden even vibronically. This vibration is an out-of-plane acetylene−phenyl bend, so it should participate in torsional motion in company with mode 15, the in-plane bend. Coriolis calculations, as shown in Table 2, make it clear that the appearance of $10b^1$ is primarily made possible by 10b borrowing intensity from this nearby 15 mode, and its appearance in several combination bands arises from the same effect. 10b also shows a broadened rotational contour consistent with its Coriolis origins. However, the intensity of the 10b band is apparently still too large relative to the 15 band intensity to be explained by the calculated coefficient. Whether this is due to nonlinearities in the multiphoton ionization process and detection or deficiencies in the calculations is not presently clear.

One set of low-energy bands with significant intensity seem to still be in question. Two closely spaced transitions are clearly observed at 555 and 561 cm^{-1}. Powers et al.[9] assigned the lower peak to βCH and the upper one to 6b, both b_2 vibrations (they stated that they followed King and So,[15] but the latter never reported a βCH band for protonated PA). However, Narayanan et al.[17] assigned the lower transition to 6b and the upper to mode 4, a b_1 vibration. Various theoretical calculations, including our own, indicate that one of the peaks must be the 6b mode, but indicate the energy for the βCH mode is in the 700−800 cm^{-1} region, making it a less likely candidate. As for mode 4, a b_1 vibration is unlikely to be as strong as the observed feature, since it would have to be induced by Coriolis coupling calculated to be at least an order of magnitude smaller than that of the weak 10b transition.

Photoelectron images using the 555 cm^{-1} resonance enabled checking the assignment for consistency with those of the PA^+ ion vibrational structure. In the PES spectrum shown in Figure 4a, a series of combination bands involving 15 and 6a modes

TABLE 3: Experimental and Theoretical Results for the Fundamental Vibrational Frequencies (cm^{-1}) of PA in the S_1 State and a Comparison with Other References

			calculations					
symmetry	Mulliken	Wilson[a]	S-A[c]	present[d]	present	King[b]	Chia[b]	mode description[c]
a_1	ν_1	νCH	3624	3325				C_8H_8 stretch
	ν_2	2	3376	3109				CH stretch
	ν_3	20a	3363	3095				CH stretch
	ν_4	7a	3342	3078				CH stretch
	ν_5	νCC	2213	2023		2061		$C_7{\equiv}C_8$ stretch
	ν_6	8a	1666	1539				CCH bend
	ν_7	19a	1535	1408	1419			CCH bend
	ν_8	13	1253	1151	1191	1191	1200	C_1C_7 stretch, CCH bend
	ν_9	9a	1230	1128	1126	1057		CCH bend
	ν_{10}	18a	1019	940	970	951	954	ring deformation
	ν_{11}	12	972	898	945	944	944	ring deformation
	ν_{12}	1	750	692	719	717	722	ring breath
	ν_{13}	6a	449	413	409	409	409	$C_7C_8H_8$−ring breath
a_2	ν_{14}	17a	697	624		728		OP CCH−ring breath
	ν_{15}	10a	615	554		656		OP CCH bend
	ν_{16}	16a	296	265	224	220		OP CCH bend
b_1	ν_{17}	5	739	666		731		OP CCH bend
	ν_{18}	17b	656	588		710		OP CCH bend
	ν_{19}	11	586	527		586		OP CCH bend
	ν_{20}	4	522	464		470		OP CCH bend
	ν_{21}	γCH	435	388				OP ring deformation
	ν_{22}	16b	321	277		362		OP ring deformation, $C_7C_8H_8$ bend
	ν_{23}	γCC	286	160	168			OP ring deformation, $C_7C_8H_8$ bend
	ν_{24}	10b	119	92	97	163		OP ring deformation, $C_7C_8H_8$ bend
b_2	ν_{25}	7b	3372	3103				CH stretch
	ν_{26}	20b	3352	3085		3079		CH stretch
	ν_{27}	8b	1824	1684	1642			ring deformation
	ν_{28}	19b	1612	1490	1442			ring deformation
	ν_{29}	14	1490	1366			1575	CCH bend
	ν_{30}	3	1391	1275	1296			CCH bend
	ν_{31}	9b	1242	1134	1152	1075		CCH bend
	ν_{32}	18b	1007	931	990	972		CCH bend
	ν_{33}	βCH	782	708				$C_7C_8H_8$ bend
	ν_{34}	6b	607	559	561	560		ring deformation
	ν_{35}	βCC	558	511	493	492		$C_1C_7C_8$ bend
	ν_{36}	15	156	160	146	322		CCH, $C_7C_8H_8$ bend

[a] The symbol ν indicates a stretch, β means an in-plane bend, and γ means an out-of-plane (OP) bend. [b] King, G. W.; So, S. P.*J. Mol. Spectrosc.* **1971**, *37*, 543. Chia, C. L.; Goodman, L. *J. Chem. Phys.* **1982**, *76*, 4745. [c] Serrano-Andres et.al. *J.Chem. Phys.* **2003**, *119*, 4294. The descriptions are the main contributions to the normal modes. The acetylene carbons are 7 and 8; C_7 is attached to the ring at C_1, while a lack of atom numbering indicates the H or C belongs to the phenyl ring. [d] From an MCSCF calculation using an augmented cc-pVDZ basis set, scaled by 0.92.

as well as the 15 mode alone are observed. On the basis of the propensity rule of ionization, if the intermediate level were the βCH mode, then the ionization would result in a series of excitations of the βCH mode in the cation state, but they are not seen in the photoelectron data. From the theoretical vibronic calculations, the intensity for the $6a^115^1$ (b_2) level should be non-negligible (0.032), and 555 cm^{-1} is the sum of the experimental values observed for the components. The $6a^115^1$ combination band is therefore believed to be the corresponding mode at 555 cm^{-1}, gaining intensity by Fermi resonance with the nearby 6b state at 561 cm^{-1}.

A moderate peak at 515 cm^{-1} not previously reported also requires further analysis. The simulation spectrum (including only the symmetry-allowed transitions) does not show this peak. From vibrational energies this peak could be assigned to either $6a^110b^1$ (b_1, 506 cm^{-1}) or $10b^2\gamma CC^2$ (a_1, 504 cm^{-1}). The choice of $10b^2\gamma CC^2$ would be favored by considerations of symmetry, but in the photoelectron imaging spectrum shown in Figure 4b we observed the series $10b^16a^n$ and $10b^26a^n$ (n = vibrational quantum number in the cation state), with no significant sign of an excitation of the γCC mode in the cation state. This then appears to be another case where the 10b mode is acquiring

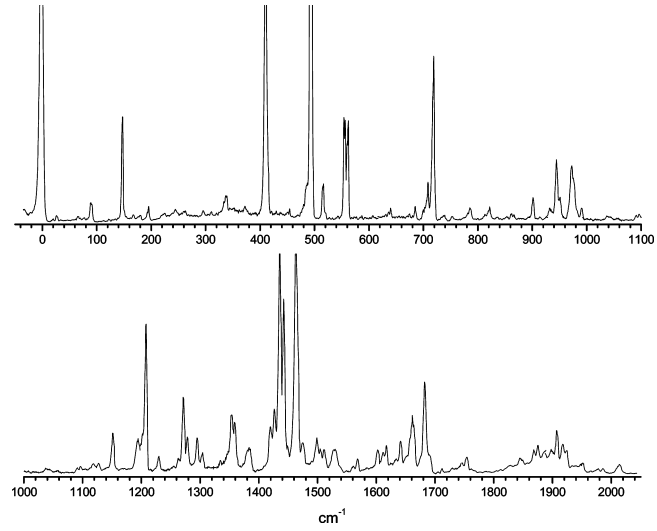

Figure 5. Expanded view of the S_1-S_0 transition showing the weak transitions. The upper trace is vertically expanded by a factor of 10 from that shown in Figure 3, while the lower trace is expanded by a factor of 3.

TABLE 4: Assignments and Relative Intensities for the Vibrational Features of Phenylacetylene in the $S_1 \leftarrow S_0$ Transition

			intensity					intensity	
freq (cm^{-1})	mode		expt	sim	freq (cm^{-1})	mode		expt	sim
0	0		2030	1118	1152	$9b^1$	b_2	190	201
97	$10b^1$	b_1	90		1193	13^1	a_1	150	157
146	15^1	b_2	490	424	1208	$\beta CC^1 1^1$	b_2	680	1228
168	γCC^1	b_1	70		1229	$6a^3$	a_1	80	3
194	$10b^2$	a_1	70	2	1271	$6b^1 1^1$	b_2	350	209
225	$16a^1$	a_2	40	5	1296	3^1	b_2	150	72
245	$10b^1 15^1$	a_2	60	0	1352	$6a^1 12^1$	a_1	260	250
295	$10b^3$	b_1	50		1383	$6a^1 18a^1$	a_1	120	3
310	γCC^2	a_1	50	13	1426	1^2	a_1	300	500
337	$10b^2 15^1$	b_2	120	4	1436	$\beta CC^1 12^1$	b_2	1050	1299
373	$\gamma CC^1 16a^1$	b_2	70	24	1442	$19b^1$	b_2	800	624
409	$6a^1$	a_1	1380	603	1463	$\beta CC^1 18a^1$	b_2	1050	1371
445	$16a^2$	a_1	60	37	1500	$6b^1 12^1$	b_2	160	274
493	βCC^1	b_2	3940	3330	1530	$6b^1 18a^1$	b_2	110	246
516	$10b^1 6a^1$	b_1	180		1569	$9b^1 6a^1$	b_2	70	29
555	$15^1 6a^1$	b_2	470	568	1603	$13^1 6a^1$	a_1	110	227
561	$6b^1$	b_2	470	32	1618	$\beta CC^1 6a^1 1^1$	b_2	130	107
639	$\beta CC^1 15^1$	a_1	60	1	1641	$8b^1$	b_2	150	18
684	$\beta CC^1 10b^2$	b_2	70	33	1660	$1^1 12^1$	a_1	250	654
707	$6b^1 15^1$	a_1	180	2	1682	$\beta CC^1 13^1$	b_2	410	960
719	1^1	a_1	760	1375	1754	$13^1 6b^1$	b_2	80	151
753	$6b^1 10b^2$	b_2	20	6	1845	$9a^1 1^1$	a_1	40	121
786	$\beta CC^1\ \gamma CC^2$	b_2	70	103	1869	$9b^1 1^1$	b_2	50	66
821	$6a^2$	a_1	70	169	1874	$\beta CC^1 6a^1 18a^1$	b_2	70	86
865	$15^1 1^1$	b_2	40	161	1885	12^2	a_1	50	108
902	$\beta CC^1 6a^1$	b_2	110	223	1908	$13^1 1^1$	a_1	100	254
945	12^1	a_1	290	551	1916	$\beta CC^1 1^2$	b_2	70	188
954	$18a^1$	a_1	260	353	1924	$18a^1 12^1$	a_1	50	20
990	$18b^1$	b_2	70	43	1951	$18a^2$	a_1	30	22
1096	$15^1 12^1$	b_2	40	197	2013	$3^1 1^1$	a_1	20	34
1119	$18a^1 15^1$	b_2	50	186					
1126	$9a^1$	a_1	50	114					

intensity by Coriolis coupling. A similar unexpected combination, $10b^1 1^1$, appears at 821 cm^{-1}.

When the intensity scale is expanded in the REMPI spectrum, there appear many weak transitions in the region of 150−400 cm^{-1}. Fundamental bands or combination bands of the low-frequency modes are possible, including 10b (97 cm^{-1}), 15 (147 cm^{-1}), γCC (155 cm^{-1}), 16a (224 cm^{-1}), and 16b (277 cm^{-1}). It is also possible that some peaks may be due to hot bands, some of which involve torsional motion of the acetylene moiety. With much less confidence because the transitions are so weak, we have assigned most of these peaks and listed them in Table 4.

In the 600−1000 cm^{-1} region, the weaker peaks can also be completely assigned. Very weak peaks at 639, 684, 707, 739, 753, 786, 821, and 865 cm^{-1} are $10a^1$, $10b^2\beta CC^1$, $6b^1 15^1$, $10a^1 10b^1$, $6a^2$, $1^1 10b^1$, and $1^1 15^1$ levels, respectively. The peaks at 902, 945, 970, and 990 cm^{-1} are $6a^1\beta CC^1$, $18a^1$, 12^1, and $18b^1$, respectively. The ordering of the equal-intensity $18a^1$ and 12^1 bands is somewhat arbitrary. Calculations put the lower one as 12, so we have followed that lead, but they are probably strongly mixed by Fermi resonance, so there is unlikely to be much meaning to that choice.

With the increasing excitation energy, the features of the spectrum display more complications that do not allow the facile assignment of transitions using only symmetry arguments and vibrational energies. However, as shown in Figure 3, the present vibronic calculations are consistent with most of the experimental results, and this means that it is possible to assign these high vibrational levels on the basis of the simulations. Even for a single peak, there are often multiple choices of vibrational levels that could be associated with this transition, but with the help of vibronic intensities, most candidates can be eliminated. The assignments in Table 4 list the strongest calculated transition near the energy of the peak in question, using experimentally assigned mode frequencies. Several weak shoulders were not assigned since Fermi resonance would render the intensities unreliable as an indicator of the mode assignment. Also, photoelectron images were not recorded in the upper energy region as line overlaps make them difficult to interpret.

Conclusions

Here we have presented the most thorough vibronic calculation done for a medium-sized molecule and compared it to an experimental spectrum in unprecedented detail. While the agreement between the experimental and theoretical intensities is not perfect (although usually within a factor of 2 except for the torsional modes), it is quite reasonable given the uncertainties in both and allows vibrational assignments for the higher energy part of the spectrum with much more confidence. Since Franck−Condon factors and vibronic coupling differ by orders of magnitude between the vibrations, a factor of 2 is usually adequate for assignment. For more isolated lines, photoelectron imaging spectroscopy gave some valuable additional information to aid in assignments. There are some indications of nonlinearities in the resonance ionization process, in that some of the weak lines show up with unexpected strength. This is not surprising, but techniques that would provide more accurate, high-resolution absorption strengths in supersonic beams are not very well developed, and resonance ionization (along with fluorescence excitation) remains the most facile method of recording these vibronic spectra with a large dynamic range.

For the calculation of individual peak intensities of an allowed transition with vibronic character, the results showed that including second-order terms has a significant effect. Further improvements in the usefulness of the calculations could be made by incorporating the effects of Fermi resonance, anharmonicity, and Born−Oppenheimer state coupling. It is also clear that if one wishes to reproduce the intensity of the weaker bands, Coriolis effects should be taken into account when appropriate.

The results presented here show that, even for the a_1 vibrations, most of the intensity comes from vibronic coupling. This is most likely the case for many other monosubstituted benzenes as well, indicating that Franck−Condon factors and calculated oscillator strengths are not useful by themselves for determining the optical properties of that class of compounds.

Acknowledgment. Work at Brookhaven National Laboratory was performed under Contract No. DE-AC02-98CH10886 with the U.S. Department of Energy and supported by its Division of Chemical Sciences, Geosciences and Biosciences.

References and Notes

(1) Sponer, H.; Wallman, S. H. *Phys. Rev.* **1940**, *57*, 1078A.
(2) Moffitt, W. *J. Chem. Phys.* **1954**, *22*, 320.
(3) Albrecht, A. C. *J. Chem. Phys.* **1960**, *33*, 156.
(4) Johnson, P. M.; Xu, H.; Sears, T. *J. Chem. Phys.* **2006**, *125*, 164330.
(5) Hofstein, J.; Xu, H.; Sears, T.; Johnson, P. *J. Phys. Chem. A* **2008**, *112*, 1195.
(6) Duschinsky, F. *Acta Physicochim. URSS* **1937**, *7*, 551.
(7) Borrelli, R.; Peluso, A. *J. Chem. Phys.* **2003**, *119*, 8437.
(8) Hohlneicher, G.; Wolf, J. *Ber. Bunsen-Ges. Phys. Chem.* **1995**, *99*, 366.
(9) Powers, D. E.; Hopkins, J. B.; Smalley, R. E. *J. Chem. Phys.* **1981**, *74*, 5971.
(10) Orlandi, G.; Siebrand, W. *Chem. Phys. Lett.* **1972**, *15*, 465.
(11) Stockburger, M.; Gattermann, H.; Klusmann, W. *J. Chem. Phys.* **1975**, *63*, 4519.
(12) Bunker, P.; Jensen, P. *Molecular Spectroscopy and Symmetry*, 2nd ed.; NRC Research Press: Ottawa, Canada, 1998.
(13) Townsend, D.; Minitti, M. P.; Suits, A. G. *Rev. Sci. Instrum.* **2003**, *74*, 2530.
(14) Dribinski, V.; Ossadtchi, A.; Mandelshtam, V. A.; Reisler, H. *Rev. Sci. Instrum.* **2002**, *73*, 2634.
(15) King, G. W.; So, S. P. *J. Mol. Spectrosc.* **1970**, *36*, 468; **1971**, *37*, 535, 543.
(16) Chia, L.; Goodman, L. *J. Chem. Phys.* **1982**, *76*, 4745.
(17) Narayanan, K.; Chang, G. C.; Shieh, K. C.; Tung, C. C.; Tzeng, W. B. *Spectrochim. Acta, Part A* **1996**, *52*, 1703.
(18) Philis, J. G.; Drougas, E.; Kosmas, A. M. *Chem. Phys.* **2004**, *306*, 253.
(19) Serrano-Andres, L.; Merchan, M.; Jablonski, M. *J. Chem. Phys.* **2003**, *119*, 4292.
(20) Wilson, E. B. *Phys. Rev.* **1934**, *45*, 706.
(21) Ribblett, J. W.; Borst, D. R.; Pratt, D. W. *J. Chem. Phys.* **1999**, *111*, 8454.

JP103449R